

面向水面溢油检测的多角度偏振反射特性 仿真研究

栾晓宁¹, 廖玉昆¹, 褚堃¹, 闫道夏¹, 牟冰¹, 秦平², 李千¹, 康颖^{1*}

¹中国海洋大学物理与光电工程学院, 山东 青岛 266100;

²中国海洋大学电子工程学院, 山东 青岛 266100

摘要 为了在耀光干扰下提升粗糙海面溢油的检测效果, 基于 Cox-Munk 粗糙海面概率统计模型, 对不同入射和观测几何下水体与油膜反射耀光的偏振度及其差异进行仿真研究。结果表明: 入射和观测几何以及海面介质的折射率是海面耀光偏振度空间分布的主要影响因素; 当满足一定太阳入射角时, 海面介质折射率差异是水/油反射耀光偏振度差出现“正负反转”的主要原因; 入射平面内水面溢油最佳偏振观测角度与太阳入射天顶角和溢油折射率相关。

关键词 测量; 线偏振度; 太阳耀光; 水面溢油; 多角度

中图分类号 O433.1

文献标志码 A

DOI: 10.3788/AOS221162

1 引言

海洋溢油事故频发以及水下石油烃自然渗漏^[1]是造成海洋溢油污染的主要原因。作为具有一定毒性的烃类污染物, 溢油能够形成覆盖于水面之上的油膜, 阻碍水体与大气间的物质交换, 对海洋生态环境和人类生产生活均构成严重威胁^[2-3]。在海洋溢油形成初期实现污染物的早期预警和连续监测, 对海洋环境安全保障工作具有重要意义^[4-7]。

海洋光学遥感是实现大面积海洋区域环境不同尺度和层次连续动态监测的有力手段, 凭借自身较高的空间分辨率、理想的持续监测能力以及适中的研制和部署成本, 在海洋环境监测领域发挥着自身独特的作用, 其接收到的辐射能量通常分为离水辐射、白帽反射和太阳耀光三部分。其中, 太阳耀光是指入射太阳光经海面镜面反射进入传感器所形成的强烈辐射信号, 是造成传感器饱和和失真的重要原因^[8], 也是长期困扰海洋光学遥感信息提取质量的固有难题之一^[9]。

传统海洋光学遥感主要依据水面目标场景反射电磁辐射能量的强度信息^[10], 而电磁波作为横波的一种, 除强度、频率(波长)和相位等属性外, 还具有偏振特性。随着遥感技术的发展, 电磁波的偏振特性逐渐为人们所重视^[11-13], 被成功应用于大气和地物相关信息的反演研究中^[14-15]。有研究表明, 包含水面介质信息的太阳耀光具有显著的偏振性质^[16-17], 而海面这类典

型的低反射率暗目标^[18]由于其折射率和表面粗糙度有别于常见水面目标物, 在太阳耀光区也能表现出一定的偏振反射特征差异^[19-20], 这为提升耀光区水面目标检测灵敏度提供了新的思路。针对基于光学偏振特征的海洋溢油检测, 国内外相继开展了一系列研究工作^[16, 21-23]; Iler 等^[24]利用改造的商业相机对水面漂浮的植物油膜进行偏振成像观测, 发现可依据可见光波段的偏振图像实现油膜污染区域的检测; 袁越明等^[25]通过对平行/垂直偏振方向光谱强度的测量, 提出了具有较高时效性的差分偏振 FTIR 水面溢油检测方法; 王峰等^[26]通过调节激光线偏振方向与入射界面之间的夹角, 根据反射光 Stokes 矢量在邦加球中移动轨迹的差异实现水面溢油污染物的检测; 申慧彦等^[27]采用多角度光谱偏振仪详细分析了入射和观测几何以及光谱探测波段对不同类型水面溢油污染物反射光谱偏振特性的影响效果; 李清灵等^[28]测量了不同种类和厚度油膜和纯净水面紫外到近红外波段的多角度偏振反射光谱, 发现油膜反射光存在明显的偏振可观测性; 李英超等^[29]采用自行搭建的室外偏振双向反射测量装置, 获得了 4 种典型海洋溢油油种的多角度偏振图像, 发现不同油种在可见光波段存在显著的偏振对比度差异。

上述研究工作表明, 在环境变量可控的理想状态下, 多角度偏振探测是一种有效的水面溢油检测手段, 但由于海洋溢油的性质和状态复杂多变, 而且在海面风速和风向影响下, 真实海面不能被视为平滑表面, 这

收稿日期: 2022-05-19; 修回日期: 2022-07-06; 录用日期: 2022-08-02; 网络首发日期: 2022-08-10

基金项目: 国家自然科学基金(61890964, 41906163, 42076183)

通信作者: kangying@ouc.edu.cn

$\cos(2\omega) = \cos \theta_s \cos \theta_v + \sin \theta_s \sin \theta_v \cos \varphi_v$ 。 (9)
构成粗糙海面的大量微小倾斜坡面的概率统计函

数与海面风速有关,且满足 Gram-Charlier 展开式^[30-31],即

$$P(Z'_X, Z'_Y) = \frac{1}{2\pi\sigma'_X\sigma'_Y} \exp\left(-\frac{\xi^2 + \eta^2}{2}\right) \cdot \left[1 - \frac{1}{2}C_{21}(\xi^2 - 1) - \frac{1}{6}C_{03}(\eta^3 - 3\eta) + \frac{1}{24}C_{40}(\xi^4 - 6\xi^2 + 3) + \frac{1}{4}C_{22}(\xi^2 - 1)(\eta^2 - 1) + \frac{1}{24}C_{04}(\eta^4 - 6\eta^2 + 3)\right], \quad (10)$$

式中: $\xi = Z'_X/\sigma'_X$; $\eta = Z'_Y/\sigma'_Y$; σ'_X 、 σ'_Y 分别为 Z'_X 和 Z'_Y 的均方根。当风速为 v_{wind} 时,针对清洁海面和水面油膜,式(10)中各参数如表 1 所示。

表 1 Gram-Charlier 参数
Table 1 Gram-Charlier parameters

Coefficient	Wind speed $v_{wind} / (\text{m} \cdot \text{s}^{-1})$	
	Clean sea surface	Floating oil slick
σ'_X	$(0.00316 \times v_{wind})^{1/2}$	$(0.003 + 0.0084 \times v_{wind})^{1/2}$
σ'_Y	$(0.003 + 0.00192 \times v_{wind})^{1/2}$	$(0.005 + 0.0078 \times v_{wind})^{1/2}$
C_{21}	$0.01 - 0.0086 \times v_{wind}$	0
C_{03}	$0.04 - 0.0033 \times v_{wind}$	0.02
C_{40}	0.40	0.36
C_{22}	0.12	0.10
C_{04}	0.23	0.26

由此,在 Cox-Munk 模型的辅助下,基于平静海面太阳耀光的正交偏振反射率 R_p 和 R_s 可得到粗糙海面反射耀光的双向偏振反射率 $R_{glint-p}$ 和 $R_{glint-s}$,即

$$R_{glint-p}(\theta_s, \theta_v, \varphi_s, \varphi_v, n, v_{wind}) = \frac{R_p(n, \theta_s, \theta_v, \varphi_s, \varphi_v)}{4 \cos^4 \beta \cos \theta_v} P(Z'_X, Z'_Y), \quad (11)$$

$$R_{glint-s}(\theta_s, \theta_v, \varphi_s, \varphi_v, n, v_{wind}) = \frac{R_s(n, \theta_s, \theta_v, \varphi_s, \varphi_v)}{4 \cos^4 \beta \cos \theta_v} P(Z'_X, Z'_Y), \quad (12)$$

式中: θ_s 、 θ_v 、 φ_s 和 φ_v 分别为太阳入射和传感器观测的天顶角和方位角; $n = n_2/n_1$ 为海面介质(清洁海面或水面油膜)相对空气的折射率。

2.3 水面溢油偏振反射模型

光波的偏振状态通常采用 Stokes 参量来表征。若入射太阳光为自然偏振光,则其 Stokes 参量为

$$\begin{bmatrix} I_i \\ Q_i \\ U_i \\ V_i \end{bmatrix} = \begin{bmatrix} E_s^2 + E_p^2 \\ 0 \\ 0 \\ 0 \end{bmatrix}, \quad (13)$$

式中: I_i 为总光谱辐亮度; Q_i 为与参考平面平行和垂直方向上的线偏振光谱辐亮度之差; U_i 为与参考平面呈 $\pm 45^\circ$ 夹角的线偏振光谱辐亮度之差; V_i 为右旋与左旋

圆偏振光谱辐亮度之差。由于通常情况下自然界中光谱的圆偏振分量值极低,一般认为 $V_i = 0$ 。

作为入射光和反射光 Stokes 参量的偏振状态变换矩阵, Mueller 矩阵能够反映介质影响和改变入射光波偏振状态的能力和效果。当光在两层均匀介质的界面上发生反射时,介质的 Mueller 矩阵 M 可表示为

$$M = \frac{1}{2} \begin{bmatrix} r_s^2 + r_p^2 & r_s^2 - r_p^2 & 0 & 0 \\ r_s^2 - r_p^2 & r_s^2 + r_p^2 & 0 & 0 \\ 0 & 0 & 2r_s r_p \cos \delta & 2r_s r_p \sin \delta \\ 0 & 0 & -2r_s r_p \sin \delta & 2r_s r_p \cos \delta \end{bmatrix}, \quad (14)$$

式中: δ 为反射区域 s 偏振与 p 偏振分量间的相位差。因此,入射太阳光与反射耀光 Stokes 参量间的变换关系为

$$\begin{bmatrix} I_o \\ Q_o \\ U_o \\ V_o \end{bmatrix} = M \begin{bmatrix} I_i \\ Q_i \\ U_i \\ V_i \end{bmatrix} = \frac{1}{2} \begin{bmatrix} (r_s^2 + r_p^2)(E_s^2 + E_p^2) \\ (r_s^2 - r_p^2)(E_s^2 + E_p^2) \\ 0 \\ 0 \end{bmatrix}. \quad (15)$$

式(15)表明,根据入射太阳光的 Stokes 参量 $[I_i, Q_i, U_i, V_i]^T$ 、水面介质的相对折射率 n 以及太阳入射天顶角 θ_s 即可计算出水面介质反射耀光的 Stokes 参量 $[I_o, Q_o, U_o, V_o]^T$ 。因此,反射耀光的线偏振度(DOLP) A_{DOLP} 为

$$A_{DOLP} = \frac{\sqrt{Q_o^2 + U_o^2}}{I_o} = \frac{r_s^2 - r_p^2}{r_s^2 + r_p^2} = \frac{R_{glint-s} - R_{glint-p}}{R_{glint-s} + R_{glint-p}}, \quad (16)$$

式中: r_p 和 r_s 分别为太阳耀光 p 分量和 s 分量的偏振反射系数。综合式(11)、(12)和(16)发现,当海面风速和风向发生改变,对倾斜坡面的概率统计函数 $P(Z'_X, Z'_Y)$ 造成影响时, $R_{glint-p}$ 和 $R_{glint-s}$ 会同时发生等幅度变化。因此,理论上海面风向和风速不会对反射耀光偏振度的空间分布造成影响。此外,为了提升模拟仿真的效率,降低程序算法的复杂性,忽略了大气散射对入射太阳光偏振状态的影响。

3 仿真模拟与结果分析

3.1 入射天顶角的影响

海面风速和风向的改变,导致粗糙海面概率统计函数发生变化,使 $R_{glint-p}$ 和 $R_{glint-s}$ 同步发生等幅度变化。

可见,风速和风向对粗糙海面反射耀光偏振度的空间分布影响有限。相比之下,太阳入射天顶角对耀光偏振度的影响效果则更为显著。

设定海面风速为 5 m/s,分别模拟入射天顶角为

15°、45°和 56°时,清洁海面($n_{\text{water}}=1.34$)和水面油膜($n_{\text{oil}}=1.64$)反射耀光的偏振度在观测空间内的分布情况,结果分别如图 2(a)~(c)及(d)~(f)所示,其中黑色点划线标明了耀光 DOLP 为 0.5 时的观测点位。

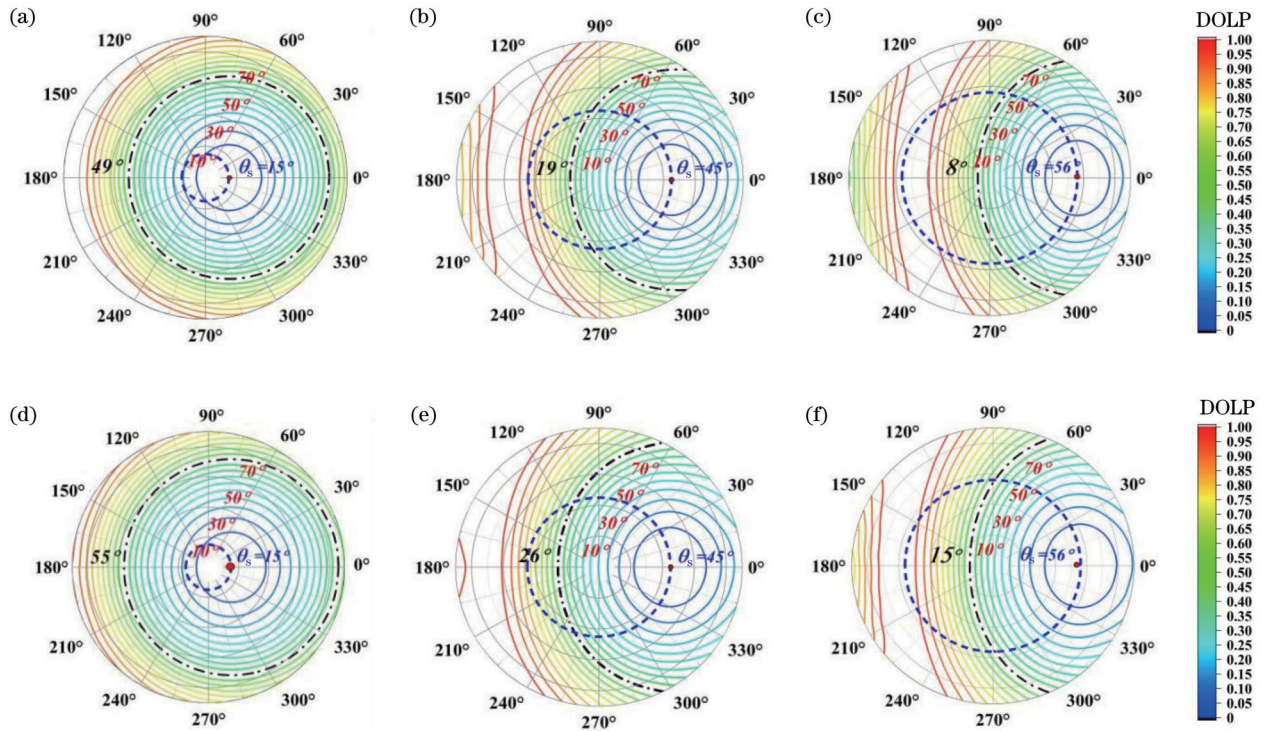


图 2 入射天顶角对清洁海面与水面溢油反射耀光 DOLP 空间分布的影响。(a) $n_{\text{water}}=1.34, \theta_s=15^\circ$; (b) $n_{\text{water}}=1.34, \theta_s=45^\circ$; (c) $n_{\text{water}}=1.34, \theta_s=56^\circ$; (d) $n_{\text{oil}}=1.64, \theta_s=15^\circ$; (e) $n_{\text{oil}}=1.64, \theta_s=45^\circ$; (f) $n_{\text{oil}}=1.64, \theta_s=56^\circ$

Fig. 2 Effect of incident zenith angle on the spatial distribution of DOLP of reflected flare from the surface of clean sea water and floating oil slick. (a) $n_{\text{water}}=1.34, \theta_s=15^\circ$; (b) $n_{\text{water}}=1.34, \theta_s=45^\circ$; (c) $n_{\text{water}}=1.34, \theta_s=56^\circ$; (d) $n_{\text{oil}}=1.64, \theta_s=15^\circ$; (e) $n_{\text{oil}}=1.64, \theta_s=45^\circ$; (f) $n_{\text{oil}}=1.64, \theta_s=56^\circ$

从图 2 可见:无论是无油清洁海面还是水面油膜,其反射太阳耀光 DOLP 极小值均位于入射主平面天顶角 θ_s 处,并以 θ_s 为中心向四周逐渐增大; θ_s 较小时, DOLP 等值线近似呈同心圆环状分布;随着 θ_s 的增大, DOLP 等值线在垂直于入射主平面方向上的等值间隔愈发超过平行方向,呈椭圆状分布。从空间分布看,反射耀光 DOLP 值较高的观测方位通常在 $90^\circ < \varphi_v < 270^\circ$ 的角度范围内;当 θ_s 较大(例如 $\theta_s \geq 45^\circ$)时,在前向反射区域内耀光 DOLP 随 θ_v 的增大而减小。

从图 2 还可发现,清洁海面和水面油膜反射耀光偏振度的空间分布均与太阳入射天顶角 θ_s 有关。当 θ_s 分别为 15°、45°和 56°时,在太阳入射平面镜面反射方向上($\varphi_v=180^\circ$),清洁海面反射耀光 DOLP 为 0.5,对应的观测天顶角 θ_v 分别为 49°、19°和 8°,而水面油膜覆盖时对应的 θ_v 分别为 55°、26°和 15°。由此可见,在太阳入射平面内, θ_s 增大的幅度与特定偏振度耀光对应的 θ_v 减小幅度相等。

3.2 介质折射率的影响

作为一种性质和状态复杂的污染物,海洋溢油具

有多变的折射率。有研究表明,非蒸馏原油的折射率通常在 1.4~1.6 范围内^[32]。为了研究海面介质折射率变化对太阳耀光 DOLP 空间分布的影响,设定太阳入射天顶角 $\theta_s=45^\circ$,对 3 种不同折射率(n_{oil} 分别为 1.44、1.54 和 1.64)的水面油膜反射耀光 DOLP 在极坐标空间内的分布情况进行仿真,结果如图 3(a)~(c)所示,其中黑色点划线标明了 3 种不同折射率油膜反射耀光 DOLP 为 0.5 时的观测点位。可以看到,不同折射率水面油膜反射耀光 DOLP 极小值均位于太阳入射主平面天顶角 θ_s 处,并以该点为中心随观测几何变化向四周逐渐增大,但耀光 DOLP 值随观测几何变化发生改变的速率和幅度与海面介质折射率有关:当观测几何发生特定角度变化时,海面介质折射率越高,耀光 DOLP 值变化的幅度越小。当 $\theta_s=45^\circ$ 时,3 种不同折射率的水面油膜反射耀光 DOLP 为 0.5 的等值线与太阳入射主平面交点对应的 θ_v 分别为 21°、24°和 26°。可见,海面介质折射率也是粗糙海面耀光偏振度空间分布的重要影响因素。考虑到清洁海面与水面油膜间的折射率差异,在特定入射和观测几何下实现水面油膜

检测和溢油类型区分在理论上具备可行性。

当 $\theta_s=45^\circ$ 时, 将清洁海面与折射率 n_{oil} 分别为 1.44、1.54 和 1.64 的水面油膜反射耀光的偏振度进行差减, 得到耀光偏振度差异 D_{DOLP} 在极坐标空间内的分布情况, 如图 3(d)~(f) 所示。可以看到, 在极坐标空间内, D_{DOLP} 的等值线以 θ_s 为中心呈条带状分布, 其中清洁海面和水面油膜反射耀光偏振度相同 ($D_{DOLP}=0$) 对应的观测点位在极坐标空间内主要分布于以下两个区域: 1) 位于后向反射区域 θ_s 处; 2) 位于 $120^\circ < \varphi_v < 240^\circ$ 方位角度范围内的“弧形”区域。其中, θ_s 附近耀光 D_{DOLP} 零值区域出现的原因是该区域的后向反射耀光均为自然偏振光, 与海面介质的折射率无关, 因此该区域内 D_{DOLP} 始终为 0。由于折射率差异, 油膜反射耀光

DOLP 随观测几何变化向四周增大的速率低于清洁海面, 导致 D_{DOLP} 值快速增大。随着 θ_v 的增大, 在 $120^\circ < \varphi_v < 240^\circ$ 观测方位内清洁海面的太阳入射角率先到达并超越布儒斯特角, 使其反射耀光 DOLP 在到达极大值后开始逐渐减小, 但此刻入射角尚未达到水面油膜的布儒斯特角, 其反射耀光 DOLP 将进一步增大并达到极大值。因此, 伴随着 θ_v 的持续增大, 水/油表面反射耀光 DOLP 变化曲线必然发生交叠, 导致 $D_{DOLP}=0$ 的“弧形”区域出现。之后, 随着 θ_v 的进一步增大, 水面油膜反射耀光 DOLP 将反超清洁海面, 产生 $D_{DOLP} < 0$ 的负值区域, 使得在极坐标空间内出现 D_{DOLP} “由正转负”的反转现象。当然, 极坐标空间内出现 D_{DOLP} 反转的前提是需要达到一定的太阳入射天顶角。

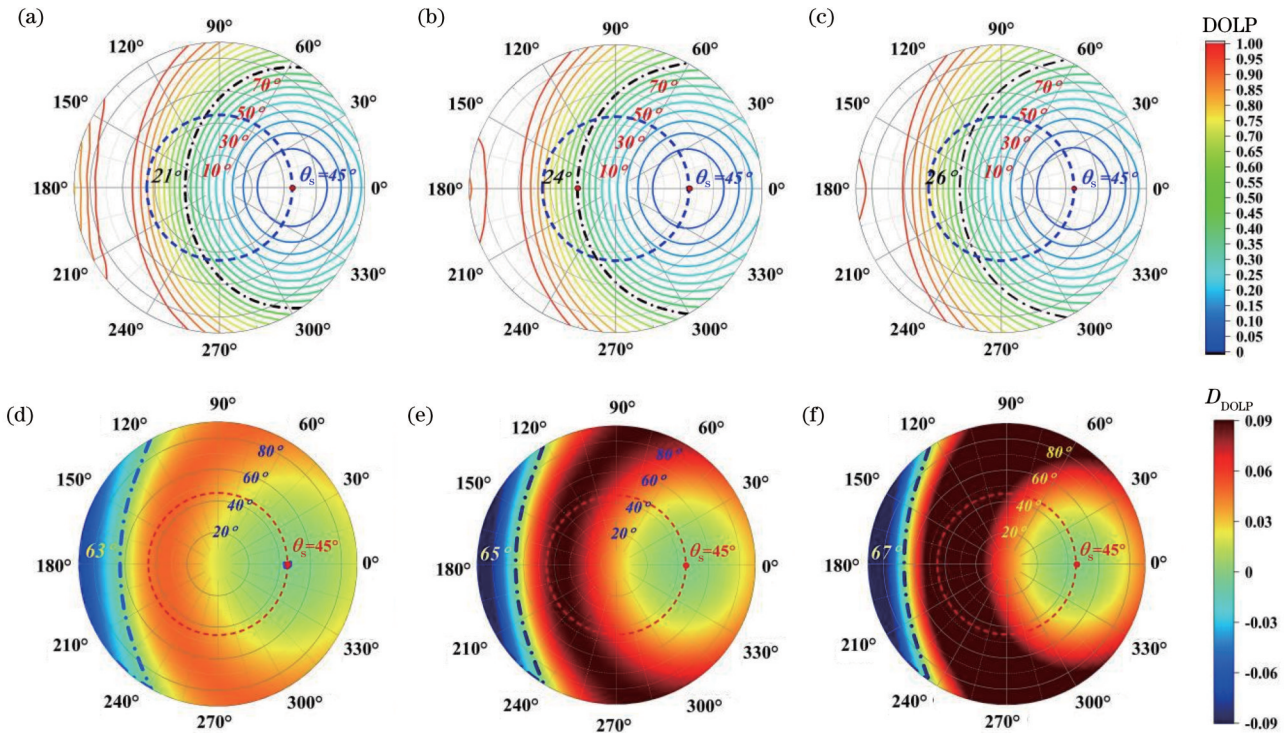


图 3 不同折射率水面油膜反射耀光 DOLP 及其与清洁海面反射耀光偏振度差 D_{DOLP} 的空间分布。(a) $n_{oil}=1.44, \theta_s=45^\circ$; (b) $n_{oil}=1.54, \theta_s=45^\circ$; (c) $n_{oil}=1.64, \theta_s=45^\circ$; (d) $n_{water}=1.34, n_{oil}=1.44$; (e) $n_{water}=1.34, n_{oil}=1.54$; (f) $n_{water}=1.34, n_{oil}=1.64$
 Fig. 3 Spatial distribution of DOLP of reflected flare from oil slick with different refractive index and relative difference D_{DOLP} with those reflected from clean water. (a) $n_{oil}=1.44, \theta_s=45^\circ$; (b) $n_{oil}=1.54, \theta_s=45^\circ$; (c) $n_{oil}=1.64, \theta_s=45^\circ$; (d) $n_{water}=1.34, n_{oil}=1.44$; (e) $n_{water}=1.34, n_{oil}=1.54$; (f) $n_{water}=1.34, n_{oil}=1.64$

3.3 水面溢油偏振检测敏感区域分析

由于溢油折射率复杂多变, 且清洁海面与水面油膜之间的折射率差异有限, 从提升水面溢油检测灵敏度的角度出发, 需针对水/油反射耀光偏振度差异最为显著的敏感观测区域开展模拟分析。由于耀光 DOLP 在极坐标空间内相对太阳入射主平面对称分布, 当入射天顶角 θ_s 为 15° , 观测方位角 φ_v 分别为 $0^\circ, 90^\circ$ (270°) 和 180° 时, 对清洁海面 ($n_{water}=1.34$) 和水面油膜 (n_{oil} 分别为 1.44、1.54 和 1.64) 反射耀光的 DOLP 随观测天顶角 θ_v 的演化曲线进行模拟, 结果如图 4(a)~(c) 所

示。可以看到, 在 $\varphi_v=0^\circ$ 的观测方位上, 随着 θ_v 的增大, 4 种不同折射率介质反射耀光 DOLP 均呈先减小后增大的变化趋势。当 $\theta_v=\theta_s=15^\circ$ 时, 4 种介质反射耀光 DOLP 均为 0, 表明该点后向反射耀光为自然偏振光, 与介质折射率无关; 但当 $\theta_v \neq \theta_s$ 时, 反射耀光的 DOLP 均大于 0, 并且在 $\theta_v > \theta_s$ 时随 θ_v 单调增大; 当 θ_s 较小 (例如 $\theta_s=15^\circ$) 时, 4 种介质反射耀光的偏振度变化曲线不会随 θ_v 的增大产生交叠。介质折射率越小, 耀光 DOLP 曲线的变化幅度越大; 折射率越大, 曲线的变化幅度越小。

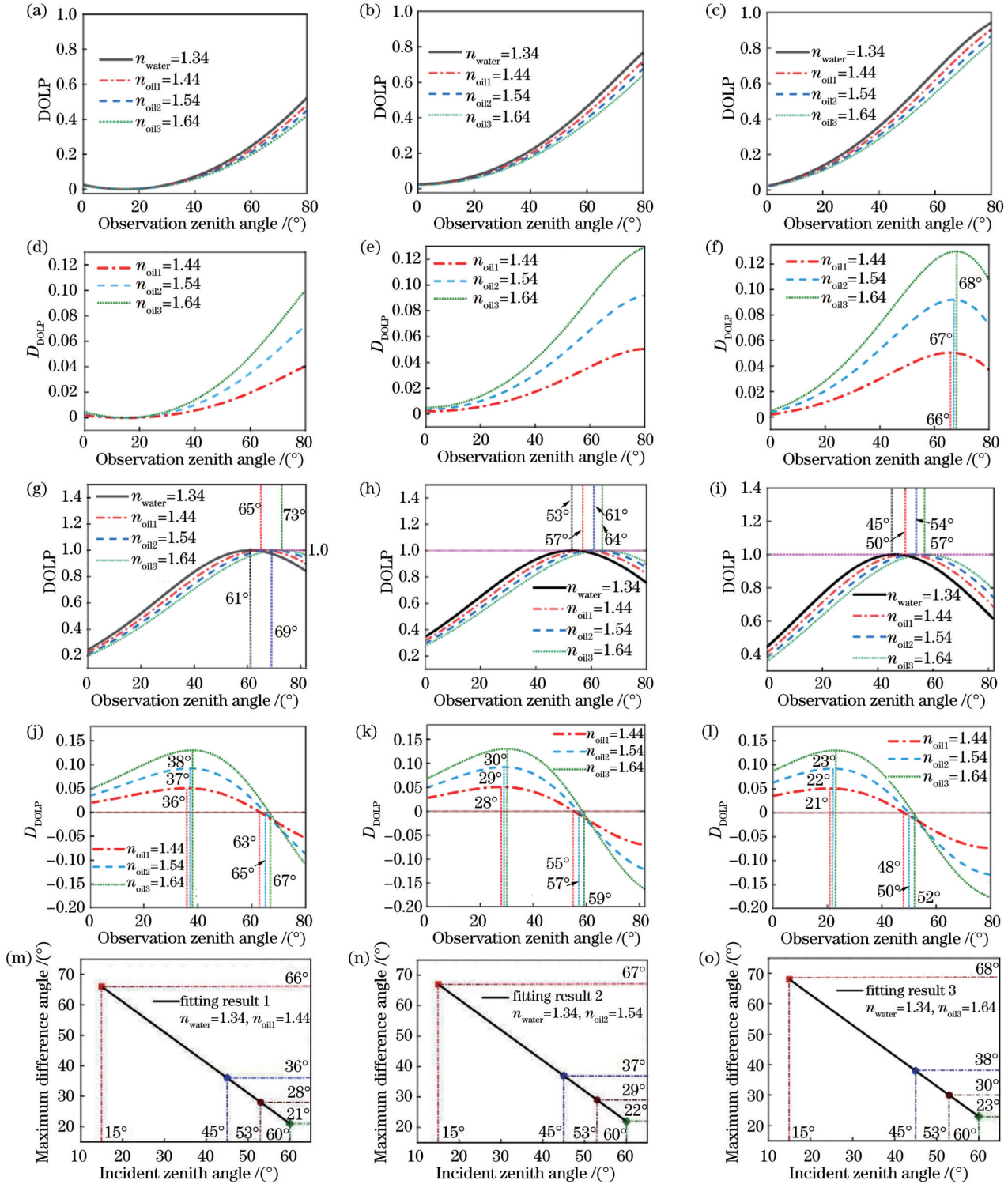


图 4 不同观测几何水/油反射耀光 DOLP 和 D_{DOLP} 空间分布及溢油敏感偏振检测角度。(a) $\theta_s=15^\circ$ 、 $\varphi_v=0^\circ$ 时的 DOLP; (b) $\theta_s=15^\circ$ 、 $\varphi_v=90^\circ$ (270°) 时的 DOLP; (c) $\theta_s=15^\circ$ 、 $\varphi_v=180^\circ$ 时的 DOLP; (d) $\theta_s=15^\circ$ 、 $\varphi_v=0^\circ$ 时的 D_{DOLP} ; (e) $\theta_s=15^\circ$ 、 $\varphi_v=90^\circ$ (270°) 时的 D_{DOLP} ; (f) $\theta_s=15^\circ$ 、 $\varphi_v=180^\circ$ 时的 D_{DOLP} ; (g) $\theta_s=45^\circ$ 、 $\varphi_v=180^\circ$ 时的 DOLP; (h) $\theta_s=53^\circ$ 、 $\varphi_v=180^\circ$ 时的 DOLP; (i) $\theta_s=60^\circ$ 、 $\varphi_v=180^\circ$ 时的 DOLP; (j) $\theta_s=45^\circ$ 、 $\varphi_v=180^\circ$ 时的 D_{DOLP} ; (k) $\theta_s=53^\circ$ 、 $\varphi_v=180^\circ$ 时的 D_{DOLP} ; (l) $\theta_s=60^\circ$ 、 $\varphi_v=180^\circ$ 时的 D_{DOLP} ; (m) $n_{oil}=1.44$ 、 $\theta_s+\theta_{vm}=81^\circ$ 时的检测角度; (n) $n_{oil}=1.54$ 、 $\theta_s+\theta_{vm}=82^\circ$ 时的检测角度; (o) $n_{oil}=1.64$ 、 $\theta_s+\theta_{vm}=83^\circ$ 时的检测角度

Fig. 4 Spatial distribution of DOLP and D_{DOLP} of solar flare reflected from surface of clean water and oil slick as well as sensitive oil slick polarization detection angle. (a) DOLP at $\theta_s=15^\circ$ and $\varphi_v=0^\circ$; (b) DOLP at $\theta_s=15^\circ$ and $\varphi_v=90^\circ$ (270°); (c) DOLP at $\theta_s=15^\circ$ and $\varphi_v=180^\circ$; (d) D_{DOLP} at $\theta_s=15^\circ$ and $\varphi_v=0^\circ$; (e) D_{DOLP} at $\theta_s=15^\circ$ and $\varphi_v=90^\circ$ (270°); (f) D_{DOLP} at $\theta_s=15^\circ$ and $\varphi_v=180^\circ$; (g) DOLP at $\theta_s=45^\circ$ and $\varphi_v=180^\circ$; (h) DOLP at $\theta_s=53^\circ$ and $\varphi_v=180^\circ$; (i) DOLP at $\theta_s=60^\circ$ and $\varphi_v=180^\circ$; (j) D_{DOLP} at $\theta_s=45^\circ$ and $\varphi_v=180^\circ$; (k) D_{DOLP} at $\theta_s=53^\circ$ and $\varphi_v=180^\circ$; (l) D_{DOLP} at $\theta_s=60^\circ$ and $\varphi_v=180^\circ$; (m) detection angle at $n_{oil}=1.44$ and $\theta_s+\theta_{vm}=81^\circ$; (n) detection angle at $n_{oil}=1.54$ and $\theta_s+\theta_{vm}=82^\circ$; (o) detection angle at $n_{oil}=1.64$ and $\theta_s+\theta_{vm}=83^\circ$

图 4(d)~(f)所示为清洁海面与 3 种不同折射率水面油膜反射耀光的偏振度差异 D_{DOLP} 随着观测天顶角 θ_v 的变化曲线。当入射天顶角 θ_s 为 15° 时,随观测天顶角 θ_v 的增大, 0° 和 90° (270°) 方位上观测到的 D_{DOLP} 均持续增大;在 $\varphi_v = 180^\circ$ 方位上, D_{DOLP} 则随着 θ_v 的增大呈现先增大后减小的变化趋势。对于折射率 n_{oil} 分别为 1.44、1.54 和 1.64 的水面油膜而言, D_{DOLP} 极大值对应的 θ_v 分别为 66° 、 67° 和 68° 。

图 4(g)~(i)所示为 $\varphi_v = 180^\circ$ 观测方位上, θ_s 分别为 45° 、 53° 和 60° 时,清洁海面与 3 种不同折射率水面油膜反射耀光的 DOLP 变化曲线。当 θ_s 较大(例如 $\theta_s = 45^\circ$) 时,随着 θ_v 的增大, 180° 观测方位上 4 种介质反射耀光的 DOLP 曲线均呈先增大后减小的变化趋势,依照折射率从小到大的顺序依次达到 DOLP 极大值后开始反向减小, DOLP 演化曲线间产生交叠。

图 4(j)~(l)所示为 $\varphi_v = 180^\circ$ 观测方位上, θ_s 分别为 45° 、 53° 和 60° 时,清洁海面与 3 种不同水面油膜反射耀光的偏振度差异 D_{DOLP} 变化曲线。可以看到,清洁海面与水面油膜间折射率差异越大, D_{DOLP} 值越高,并且随着 θ_v 增大呈现先增大后减小的变化趋势。当 θ_s 为 45° 时, $\varphi_v = 180^\circ$ 方位上清洁海面与 3 种不同折射率油膜 D_{DOLP} 极大值对应的观测天顶角 θ_{vm} 分别为 36° 、 37° 和 38° ; 当 θ_s 分别为 53° 和 60° 时,对应的 θ_{vm} 分别为 28° 、 29° 、 30° 和 21° 、 22° 、 23° 。

图 4(m)~(o)所示为 D_{DOLP} 极大值对应的 θ_{vm} 与 θ_s 的拟合关系。可以看到,无论 θ_s 如何变化,其与耀光偏振度差值 D_{DOLP} 极大值对应的观测天顶角 θ_{vm} 呈线性负相关关系,即 θ_s 与 θ_{vm} 之和为固定值。当水面油膜折射率 n_{oil} 分别为 1.44、1.54 和 1.64 时, θ_s 与 θ_{vm} 之和分别为 81° 、 82° 和 83° 。该结果表明在太阳入射主平面内,当入射天顶角 θ_s 与观测天顶角 θ_v 之和分别为 81° 、 82° 和 83° 时,针对折射率 n_{oil} 分别为 1.44、1.54 和 1.64 水面油膜的偏振检测灵敏度最高。

4 结 论

采用 Fresnel 定律中定义的偏振反射参数,在 Cox-Munk 粗糙海面概率统计模型的辅助下,对不同入射和观测几何下清洁海面与 3 种不同折射率水面油膜反射耀光 DOLP 及其空间分布进行了仿真模拟和对比分析,量化总结了入射和观测几何以及介质折射率变化对水/油反射耀光偏振度差异 D_{DOLP} 的影响程度和变化规律,并确定了不同折射率水面溢油的最佳偏振检测角度。相关结果表明:与海面风向和风速不同,入射和观测几何及水面介质折射率是海面耀光 DOLP 空间分布的主要影响因素;水面介质折射率越小,反射耀光 DOLP 随观测几何角度改变而发生变化的速率越高;如果太阳入射天顶角较小时,清洁海面反射耀光的 DOLP 在整个观测空间内始终超过水面溢油,只有当入射天顶角达到一定角度后,才有可能在耀光前向反射区域

特定观测方位角范围内观测到水/油反射耀光偏振度“正负反转”现象;对于特定折射率的水面油膜,其水/油反射耀光偏振度差异最显著时对应的最佳偏振检测角度与太阳入射天顶角之和为常量,且该常量与油膜折射率有关。从仿真模拟的结果看,在特定入射和观测几何条件下,偏振检测技术可基于水面介质折射率差异提升水面溢油检测灵敏度,体现了多角度偏振遥感探测技术的特点和潜力,有望为海洋环境安全保障工作的开展提供更加有力的方法依据和技术支撑。

参 考 文 献

- [1] Hu C M, Li X F, Pichel W G, et al. Detection of natural oil slicks in the NW Gulf of Mexico using MODIS imagery[J]. *Geophysical Research Letters*, 2009, 36(1): L01604.
- [2] Corsellis Y Y, Krasovec M M, Sylvi L L, et al. Oil removal and effects of spilled oil on active microbial communities in close to salt-saturation brines[J]. *Extremophiles*, 2016, 20(3): 235-250.
- [3] Miralles G, Nerini D, Manté C, et al. Effects of spilled oil on bacterial communities of Mediterranean coastal anoxic sediments chronically subjected to oil hydrocarbon contamination[J]. *Microbial Ecology*, 2007, 54(4): 646-661.
- [4] Mariano A J, Kourafalou V H, Srinivasan A, et al. On the modeling of the 2010 Gulf of Mexico oil spill[J]. *Dynamics of Atmospheres and Oceans*, 2011, 52(1/2): 322-340.
- [5] Jha M N, Levy J, Gao Y. Advances in remote sensing for oil spill disaster management: state-of-the-art sensors technology for oil spill surveillance[J]. *Sensors*, 2008, 8(1): 236-255.
- [6] Kessler J D, Valentine D L, Redmond M C, et al. Response to Comment on: a persistent oxygen anomaly reveals the fate of spilled methane in the deep Gulf of Mexico[J]. *Science*, 2011, 332(6033): 1033-1033.
- [7] Leifer I, Clark J F, Chen R F. Modifications of the local environment by natural marine hydrocarbon seeps[J]. *Geophysical Research Letters*, 2000, 27(22): 3711-3714.
- [8] Kay S, Hedley J, Lavender S. Sun glint correction of high and low spatial resolution images of aquatic scenes: a review of methods for visible and near-infrared wavelengths[J]. *Remote Sensing*, 2009, 1(4): 697-730.
- [9] Wang M H, Bailey S W. Correction of Sun glint contamination on the SeaWiFS ocean and atmosphere products[J]. *Applied Optics*, 2001, 40(27): 4790-4798.
- [10] 李煜, 陈杰, 张渊智. 合成孔径雷达海面溢油探测研究进展[J]. *电子与信息学报*, 2019, 41(3): 751-762.
Li Y, Chen J, Zhang Y Z. Progress in research on marine oil spills detection using synthetic aperture radar[J]. *Journal of Electronics & Information Technology*, 2019, 41(3): 751-762.
- [11] 史浩东, 王稼禹, 李英超, 等. 复杂海况下海洋生态环境多维度光学监测方法[J]. *光学学报*, 2022, 42(6): 0600004.
Shi H D, Wang J Y, Li Y C, et al. Multi-dimensional optical monitoring method of marine ecological environment under complex sea conditions[J]. *Acta Optica Sinica*, 2022, 42(6): 0600004.
- [12] 何玉青, 姜梦蝶, 胡秀清, 等. 基于洋面场景的 MERSI 偏振辐射特性反演及其分析方法[J]. *光学学报*, 2022, 42(6): 0628002.
He Y Q, Jiang M D, Hu X Q, et al. Retrieval and analysis of MERSI polarization radiation characteristics based on ocean scene[J]. *Acta Optica Sinica*, 2022, 42(6): 0628002.
- [13] 王荣昌, 王峰, 任帅军, 等. 基于双流融合网络的单兵伪装偏振成像检测[J]. *光学学报*, 2022, 42(9): 0915001.
Wang R C, Wang F, Ren S J, et al. Polarization imaging detection of individual camouflage based on two-stream fusion network[J]. *Acta Optica Sinica*, 2022, 42(9): 0915001.

- [14] 程天海, 顾行发, 陈良富, 等. 卷云多角度偏振特性研究[J]. 物理学报, 2008, 57(8): 5323-5332.
Cheng T H, Gu X F, Chen L F, et al. Multi-angular polarized characteristics of cirrus clouds[J]. Acta Physica Sinica, 2008, 57(8): 5323-5332.
- [15] 程天海, 顾行发, 余涛, 等. 地表双向反射对天基矢量辐射探测的影响分析[J]. 物理学报, 2009, 58(10): 7368-7375.
Cheng T H, Gu X F, Yu T, et al. Effect of surface reflectances on the space-based vector radiative detection[J]. Acta Physica Sinica, 2009, 58(10): 7368-7375.
- [16] Mobley C D. Polarized reflectance and transmittance properties of windblown sea surfaces[J]. Applied Optics, 2015, 54(15): 4828-4849.
- [17] Harmel T, Hieronymi M, Slade W, et al. Laboratory experiments for inter-comparison of three volume scattering meters to measure angular scattering properties of hydrosols[J]. Optics Express, 2016, 24(2): A234-A256.
- [18] 张卫国. 海面太阳耀光背景下的偏振探测技术[J]. 中国光学, 2018, 11(2): 231-236.
Zhang W G. Application of polarization detection technology under the background of sun flare on sea surface[J]. Chinese Optics, 2018, 11(2): 231-236.
- [19] Cooper A W, Lentz W J, Walker P L, et al. Infrared polarization measurements of ship signatures and background contrast[J]. Proceedings of SPIE, 1994, 2223: 300-309.
- [20] Cooper A W, Lentz W J, Walker P L. Infrared polarization ship images and contrast in the MAPTIP experiment[J]. Proceedings of SPIE, 1996, 2828: 85-96.
- [21] 陈卫, 孙晓兵, 乔延利, 等. 海面耀光背景下的目标偏振检测[J]. 红外与激光工程, 2017, 46(S1): S117001.
Chen W, Sun X B, Qiao Y L, et al. Polarization detection of marine targets covered in glint[J]. Infrared and Laser Engineering, 2017, 46(S1): S117001.
- [22] 陈兴峰, 顾行发, 程天海, 等. 真实海洋表面的太阳耀光偏振辐射特性仿真与分析[J]. 光谱学与光谱分析, 2011, 31(6): 1648-1653.
Chen X F, Gu X F, Cheng T H, et al. Simulation and analysis of polarization characteristics for real sea surface sunglint[J]. Spectroscopy and Spectral Analysis, 2011, 31(6): 1648-1653.
- [23] 刘志刚, 周冠华. 太阳耀光的偏振分析[J]. 红外与毫米波学报, 2007, 26(5): 362-365.
Liu Z G, Zhou G H. Polarization of Sun glint[J]. Journal of Infrared and Millimeter Waves, 2007, 26(5): 362-365.
- [24] Iler A L, Hamilton P D. Detecting oil on water using polarimetric imaging[J]. Proceedings of SPIE, 2015, 9459: 94590P.
- [25] 袁越明, 熊伟, 方勇华, 等. 差分偏振 FTIR 光谱法探测水面溢油污染的模型分析[J]. 红外与激光工程, 2011, 40(3): 408-412.
Yuan Y M, Xiong W, Fang Y H, et al. Modeling analysis of detection of oil spills on water by differential polarization FTIR spectrometry[J]. Infrared and Laser Engineering, 2011, 40(3): 408-412.
- [26] 王峰, 杨锦宏, 李小明, 等. 水面溢油可见/近红外偏振光检测方法研究[J]. 激光与光电子学进展, 2012, 49(5): 051202.
Wang F, Yang J H, Li X M, et al. Oil spill visible/near-infrared polarized light detection method[J]. Laser & Optoelectronics Progress, 2012, 49(5): 051202.
- [27] 申慧彦, 周浦城, 王峰. 水面溢油污染的多角度多波段偏振特性研究[J]. 海洋环境科学, 2012, 31(2): 241-245, 249.
Shen H Y, Zhou P C, Wang F. Multi-angle and multi-band polarimetric characteristic of spilled oil pollution on water surface[J]. Marine Environmental Science, 2012, 31(2): 241-245, 249.
- [28] 李清灵, 尹达一. 椭偏测量法的油膜紫外可见-近红外光谱光谱偏振特性研究[J]. 光谱学与光谱分析, 2019, 39(6): 1661-1666.
Li Q L, Yin D Y. A study of spectral polarization properties of oil slick with ellipsometry from ultraviolet to near-infrared[J]. Spectroscopy and Spectral Analysis, 2019, 39(6): 1661-1666.
- [29] 李英超, 刘嘉楠, 史浩东. 基于偏振特性的海洋溢油物种识别研究[J]. 光子学报, 2021, 50(7): 0712001.
Li Y C, Liu J N, Shi H D. Research on identification of marine oil spill based on polarization characteristics[J]. Acta Photonica Sinica, 2021, 50(7): 0712001.
- [30] Takashima T, Masuda K. Degree of radiance and polarization of the upwelling radiation from an atmosphere-ocean system[J]. Applied Optics, 1985, 24(15): 2423-2429.
- [31] Kawata Y, Yamazaki A. Multiple scattering analysis of airborne POLDER image data over the sea[J]. IEEE Transactions on Geoscience and Remote Sensing, 1998, 36(1): 51-60.
- [32] Aripnammal S. A novel method of using refractive index as a tool for finding the adulteration of oils[J]. Research Journal of Recent Sciences, 2012, 1(7): 77-79.

Simulation Investigation of Multi-Angle Polarization Reflection Characteristics for Marine Oil Spill Detection

Luan Xiaoning¹, Liao Yukun¹, Zhuo Kun¹, Yan Daoxia¹, Mu Bing¹, Qin Ping², Li Qian¹, Kang Ying^{1*}

¹College of Physics and Opto-Electronic Engineering, Ocean University of China, Qingdao 266100, Shandong, China;

²College of Electronic Engineering, Ocean University of China, Qingdao 266100, Shandong, China

Abstract

Objective As a toxic hydrocarbon pollutant, oil spills can become oil slicks on the sea surface, which hinders the material exchange between water and air and poses a serious threat to marine ecological environments as well as the production and life of human beings. Investigation on how to realize early warning and continuous monitoring of pollutants in the early stage of oil spill accidents is of great significance to the protection of marine environments. The marine optical remote sensor is a powerful tool to realize continuous dynamic monitoring of large-area marine environments at different scales and levels. But the solar flare which is the main reason for the saturation and distortion of optical remote sensors brings

inherent difficulties in improving information extraction of remote sensing. Some previous studies indicate that the solar flare possesses significant polarization characteristics under specific conditions, and polarization detection is an effective method for oil spill detection. However, under the influence of wind speed and direction, the real sea surface cannot be regarded as a smooth one, and the characteristics and states of oil spills are complex. In the 1950s, Charles Cox and Walter Munk put forward a famous Cox-Munk probabilistic statistical model of rough sea surface after a long-term rigorous investigation, which conforms very well to the real state of the sea surface. In this paper, the Cox-Munk probabilistic statistical model is employed to model the solar flare reflected by rough sea surface affected by wind speed and direction. With the polarization reflection parameter defined by Fresnel's law, this paper quantitatively simulates and studies the spatial distribution and related differences between the degree of linear polarization (DOLP) of solar flare reflected by clean seawater and oil slicks with different refractive indexes under different incident and observation geometries, as well as different wind speed and direction on the sea surface. This paper hopes that the simulation results can facilitate the application of multi-angle polarization remote sensing technology for marine oil spill surveillance.

Methods Firstly, with the polarization reflectance coefficients defined by Fresnel's law, the orthogonal polarization Fresnel reflectance R_p and R_s of the solar flare reflected by calm sea surface are obtained. According to Cox-Munk probabilistic statistical model, the polarization bidirectional reflectance $R_{\text{glint-p}}$ and $R_{\text{glint-s}}$ of the solar flare reflected by rough sea surface are calculated based on R_p and R_s . In the next step, on the basis of $R_{\text{glint-p}}$ and $R_{\text{glint-s}}$, the spatial distribution of the DOLP of the solar flare reflected by different sea surface media with various refractive indexes on rough sea surface affected by different wind speed and direction is simulated with respect to any incident and observation geometry. Furthermore, the spatial distribution of DOLP differences between clean seawater and oil slicks is simulated, and the most sensitive polarization observation angle of oil slicks with different refractive indexes is obtained.

Results and Discussions The wind speed is set at 5 m/s, with the incident zenith angle set as 15° , 45° , and 56° , and the spatial distribution of the DOLP of the solar flare reflected by clean seawater and oil slicks is simulated (Fig. 2). The contour of the DOLP of the solar flare is approximately a concentric circle, and the minimum of the DOLP is located at the position corresponding to the incident zenith angle within the incident principal plane. As the incident angle gets larger, the distance between the DOLP contour in the direction perpendicular to the incident principal plane is wider than that in the parallel direction, and the contour features an elliptic shape. According to a specific DOLP of the solar flare, within the incident principal plane, the increase in θ_s is equal to the decrease in θ_v . By making the solar incident angle θ_s is 45° , this paper simulates the distribution of the DOLP of the solar flare reflected by oil slicks with three different refractive indexes (Fig. 3). It is shown that the variation rate of the DOLP value with the change in observation geometry is related to the refractive index of sea surface media. When a specific angle is changed in the observation geometry, as the refractive index of sea surface media increases, the variation of the DOLP value becomes slight. In order to improve the oil slick detection sensitivity, the optimum polarization detection area with the largest difference between the DOLP of the solar flare reflected by clean seawater and oil slicks is simulated. When the incident zenith angle $\theta_s = 45^\circ$, and the observation azimuth angle φ_v equals 0° and 180° or ranges from 90° to 270° , respectively, the DOLP variation curves with the observation zenith angle φ_v of the solar flare reflected by clean seawater and oil slicks are simulated and compared (Fig. 4). When the incident angle is big enough, as observation zenith angle increases, the DOLP curves of all media first increase and then decrease. In addition, no matter how θ_s changes, there is a negative linear correlation between θ_s and the observation zenith angle θ_{vm} corresponding to the most significant DOLP difference between the solar flare reflected by clean seawater and oil slicks. That means the sum of θ_s and θ_{vm} is a fixed value, which is highly related to the refractive index of oil slicks.

Conclusions In this paper, the spatial distribution of DOLP of the solar flare reflected by clean seawater and oil slicks are simulated under various incident and observation geometries based on Cox-Munk probabilistic statistical model. The optimum polarization detection angle of oil slicks with different refractive indexes is determined. It is shown that the incident and observation geometry as well as the refractive index of sea surface media are the main factors affecting the spatial distribution of the DOLP of the solar flare. Furthermore, a lower refractive index of the medium is often accompanied by a higher rate of variation of the DOLP of the solar flare with specific changes in the observation geometry. When the incident zenith angle reaches a certain value, it is possible to observe a positive-to-negative reversal of the difference between the DOLP of the solar flare reflected by seawater and oil slicks within a specific range of azimuth angles of the forward reflection area. For oil slicks with specific refractive indexes, the sum of the optimum polarization detection angle and the solar incident zenith angle is constant, which is closely related to the refractive index of the oil slicks. According to the simulation results, under specific incident and observation geometry, polarization detection can significantly improve the sensitivity of oil spill detection. Therefore, this paper is expected to provide support for the protection of marine environments.

Key words measurement; degree of linear polarization (DOLP); solar flare; oil slick; multiple angles